**THE EUROPEAN
PHYSICAL JOURNAL E**

Regular Article

Cassie-Baxter to Wenzel state wetting transition: Scaling of the front velocity

A.M. Peters[1,5], C. Pirat[2,3,5], M. Sbragaglia[2,4,5], B.M. Borkent[2,5], M. Wessling[1,5], D. Lohse[2,5], and
R.G.H. Lammertink[1,5,a]

[1] Membrane Technology Group, Faculty of Science and Technology, Mesa+ Institute for Nanotechnology, University of Twente,
  P.O. Box 217, 7500 AE Enschede, The Netherlands
[2] Physics of Fluids, Faculty of Science and Technology, Mesa+ Institute for Nanotechnology, University of Twente, P.O. Box 217,
  7500 AE Enschede, The Netherlands
[3] Laboratoire de Physique de la Matière Condensée et Nanostructures, Université de Lyon, Univ. Lyon I, CNRS, UMR 5586,
  69622 Villeurbanne, France
[4] Department of Physics, University of Rome Tor Vergata, Via della Ricerca Scientifica 1, 00133 Rome, Italy
[5] Impact, Institute on Mechanics, Processes and Control Twente, University of Twente, P.O. Box 217, 7500 AE Enschede,
  The Netherlands

Abstract. We experimentally study the dynamics of water in the Cassie-Baxter state to Wenzel state
transition on surfaces decorated with assemblies of micrometer-size square pillars arranged on a square
lattice. The transition on the micro-patterned superhydrophobic polymer surfaces is followed with a high-
speed camera. Detailed analysis of the movement of the liquid during this transition reveals the wetting
front velocity dependence on the geometry and material properties. We show that a decrease in gap
size as well as an increase in pillar height and intrinsic material hydrophobicity result in a lower front
velocity. Scaling arguments based on balancing surface forces and viscous dissipation allow us to derive
a relation with which we can rescale all experimentally measured front velocities, obtained for various
pattern geometries and materials, on one single curve.

PACS. 68.03.Cd Surface tension and related phenomena – 68.08.Bc Wetting – 68.08.De Liquid-solid
interface structure: measurements and simulations

1 Introduction

The interaction between water and a hydrophobic ma-
terial has attracted considerable interest in recent years.
In particular, much effort has been devoted to mimic
the superhydrophobic properties often encountered in
nature [1–4]. The water-repelling feature, also called the
Lotus effect, is attributed to the material's intrinsic hy-
drophobicity together with its surface roughness [5,6].
Micro-pillars are often used to resemble the natural rough-
ness of a superhydrophobic lotus leaf. In general, a drop of
water on a hydrophobic solid surface can experience two
distinct states: suspended on a composite surface of mate-
rial and air pockets (Cassie-Baxter state [7]) or following
all the contours of the rough surface (Wenzel state [8]).
For these two states the macroscopic contact angle and
the contact angle hysteresis are different as compared to
the flat hydrophobic surface. Due to the small solid-liquid

contact area in the Cassie-Baxter state, the hysteresis is
very small and a liquid drop can roll off easily. In the
Wenzel state the apparent contact angle is determined
by the roughness of the material and the hysteresis is
larger as the liquid follows the contours of the surface.
Theoretical analysis [9–11] has shown that the state with
a smaller contact angle corresponds to a lower-energy
level. The presence of energy barriers between the two
states may prevent a spontaneous transition and exter-
nal forces have to be applied in order to induce the tran-
sition from the higher-energy (metastable Cassie-Baxter)
state to the lower-energy (Wenzel) state [12–15]. Based on
experiments with micro-patterned surfaces, many design
criteria have been proposed to control these two wetted
states as well as the transition of one to the other [16–22].
Geometry and surface properties can be tuned to either
keep a liquid in the suspended state (to minimize hydrody-
namic friction) or wet the complete surface (to increase the
contact area between the liquid and the solid) [16,23–25].
In the present work, patterns of micrometer-size pillars

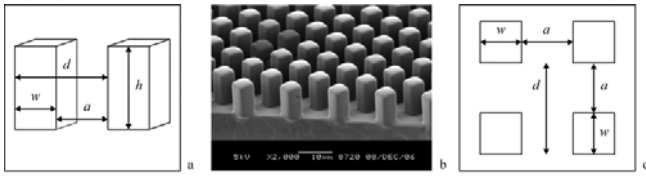ᵃ e-mail: `r.g.h.lammertink@utwente.nl`

Fig. 1. (a) Illustration of a side view of two pillars with pillar width w, pillar height h, gap size between the pillars a and wavelength d. (b) SEM picture of a micro-patterned polymer (Kraton$^{\text{TM}}$ D-1102CS) film with gap size $5\,\mu$m and pillar height $10\,\mu$m. (c) Illustration of the top view of four pillars: square pillars in a square array.

Table 1. Gap sizes a of used molds (μm).

Field	Mold 1 (Kraton)	Mold 2 (PDMS)
1	2	16
2	5	18
3	8	20
4	11	22
5	14	24
6	17	26

arranged on a square lattice are considered (fig. 1). The sketches of the side and top view of the pattern (figs. 1a and c, respectively) illustrate its geometrical parameters: pillar width w, pillar height h, gap size between the pillars a and wavelength $d = a + w$. For the movement of a liquid front between two micro-pillars, energy is gained by a reduction of the free liquid-gas interface suspended on top of the pillars ($\sigma_{LG}\, a\, \mathrm{d}x$), but energy is lost in wetting the hydrophobic walls ($\sigma_{LG}\,(2h + a)\mathrm{d}x \cos\theta$). Balancing these energies defines a critical point, which can be expressed in terms of geometrical parameters of the micro-pattern and of the materials intrinsic contact angle with water θ (see also eqs. (1) and (2) in [23]). This critical point can be expressed in terms of a critical contact angle θ_c

$$\cos\theta_c = -1 + \frac{2h}{2h + a},\qquad(1)$$

with h the pillar height and a the gap size between the pillars. For $\cos\theta_c < \cos\theta < 0$, front propagation after initial propagation is energetically favored, whereas for $\cos\theta < \cos\theta_c$ any front will stop. For comparison of the results in this paper, the critical point is rewritten in terms of the critical gap size a_c

$$a_c = \frac{2h}{\cos\theta + 1} - 2h.\qquad(2)$$

When $a > a_c$, front propagation is energetically favored, whereas for $a < a_c$ any front will stop. Only recently, the dynamics of the wetting transition (from Cassie-Baxter to Wenzel) has been revealed by observing the liquid interface as it collapses and wets the area between the micro-pattern [14,23,26]. During the transition, a zipping wetting mechanism was observed for small gap sizes [23,26–29]. The front propagates in a step-wise manner, filling row by row. For larger gap sizes, the propagation is faster with a more circular wetted area. With these observations in mind, we define two regimes: the zipping and the non-zipping regime. In the zipping regime, the velocity in one direction (to advance to the next row) is much smaller than the velocity in the other direction (liquid filling up one row). In the non-zipping regime, both velocities are more comparable. In this paper we investigate the influence of several parameters on the liquid front velocity during the Cassie-Baxter to Wenzel state wetting transition. The wetting front has been followed experimentally

on various micro-patterns with different a, h, and θ values. To extrapolate these findings to other geometries or materials, a scaling argument for the front velocity is derived.

2 Experimental

2.1 Preparation of the molds

Molds were prepared in the cleanroom by standard photolithography and deep reactive ion etching on silicon wafers. Each mold contains fields ($20\,\text{mm} \times 20\,\text{mm}$) filled with $5\,\mu$m wide square holes (w) in a regular square array with gap sizes between the holes (a) varying from 2 to $26\,\mu$m. Two mold types are defined in table 1: mold type 1 was used as is for replicating Kraton$^{\text{TM}}$ films and mold type 2 was hydrophobized enabling an easy release of thin PDMS films. The depth of the mold (equal to the height h of the pillars) was also varied. Four copies of mold type 1 were etched to different depths: 4.4, 10, 14 and $15.6\,\mu$m. The final depths of two copies of mold type 2 were 4.7 and $8\,\mu$m. The result is a variety of combinations of gap sizes and pillar heights. The geometrical sizes were taken from scanning electron microscopy pictures ($5\,$kV, JSM 5600LV, JEOL) of the polymer films, not from the molds. Prior to imaging, the films were broken in liquid nitrogen and sputtered with a $30\,$nm gold layer (SCD 040, Balzers Union). All molds of type 2 were coated with a hydrophobic FOTS coating (1H,1H,2H,2H-perfluorooctyltrichlorosilane, Fluka Chemicals). The coating procedure was as follows: a silicon wafer was placed in a large petridish with a drop of FOTS next to the wafer. The covered petridish was placed in an oven for 2 hours at $120\,^{\circ}$C to evaporate the FOTS and to deposit the FOTS molecules onto the substrate. This was followed by an annealing step at $100\,^{\circ}$C for 1 hour. The wafers were washed with isopropanol (analysis grade, Merck), MilliQ water and again isopropanol and dried under a flow of nitrogen.

2.2 Preparation of the polymer films

All materials were used as received, *i.e.* without any further purification. Two types of polymers were used for casting micro-patterned films: Kraton$^{\text{TM}}$ D-1102CS (a linear styrene-butadiene-styrene block copolymer with 29.5 wt% styrene, Kraton Polymers) and PDMS (polydimethylsiloxane, RTV 615 rubber component A and
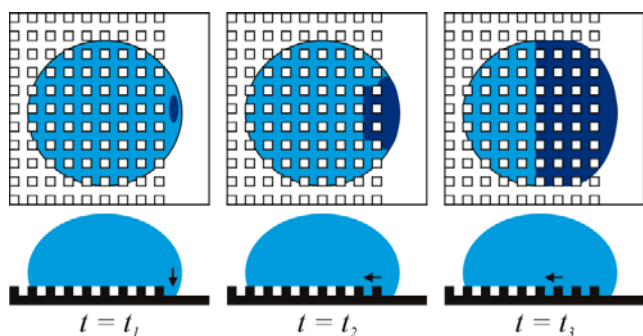
Fig. 2. Three images illustrating the spreading of the liquid between the pillars in the zipping regime in time (bottom and side views, not to scale). Left: the base of a drop hangs over the edge of an array of pillars and touches the flat surface at $t = t_1$. Middle: the first row is filled at $t = t_2$. Right: the liquid is moving between the pillars from the third to the fourth row at $t = t_3$. The liquid slows down significantly when reaching the edge of the drop base.

curing agent B, GE Bayer Silicones). The Kraton was dissolved in toluene (analysis grade, Merck) to make a 30 wt% solution, which was stirred overnight. The solution was cast on an untreated mold (type 1) with a thickness of 200–300 μm. The toluene was allowed to evaporate overnight before releasing the micro-patterned film with ethanol (analysis grade, Merck). Films were dried and stored in a 30 °C vacuum oven until use. The static contact angle for water on a flat Kraton film was 100°. The micro-patterned films exhibited contact angles around $147 \pm 1°$ for liquid in the Cassie-Baxter state. These values were measured with an optical contact angle measuring instrument (OCA 20, Dataphysics) by suspending a 6 μl drop on the surface. To obtain a PDMS mixture, the rubber component A was mixed with the curing agent B (10:1 w/w) and degassed before use. The liquid was cast on a hydrophobized mold (type 2) with a thickness of 100–300 μm and cured in an oven for 3 hours at 60 °C. The static contact angle for water on flat PDMS was 120° and on the micro-patterned PDMS between 157° and 161° (Cassie-Baxter state). Each micro-patterned field was cut out and placed on a 170 μm thick microscope slide before use.

2.3 Optical microscopy and high-speed imaging

The transition from the Cassie-Baxter state to the Wenzel state is observed from the bottom through the microscope slide and the translucent film by an inverted microscope in combination with high-speed imaging. Figure 1b shows a scanning electron microscopy (SEM) picture of a typical micro-patterned polymer film with square pillars in a square array. The experimental procedure of measuring the filling dynamics is discussed in earlier work [26]. By placing the drop completely on an array of pillars, the initiation time as well as the initial location strongly vary. To control the initiation point and time of the transition, the water drop is placed at the edge of the patterned area (fig. 2). Initial spreading now occurs at the flat surface,
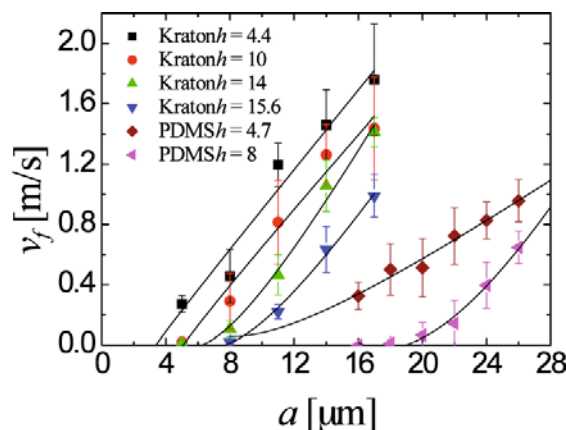

Fig. 3. Front velocity v_f *versus* gap size a for Kraton ($\theta \simeq 100°$) and PDMS ($\theta \simeq 120°$) at different pillar heights h (given in μm, see legend). In order to estimate the critical gap size a_c from these experimental data, each data set is fitted to eq. (16) and the fits (solid lines) are then extrapolated to $v_f = 0$ m/s. The obtained values of a_c are shown in table 2 and compared with the theoretical expectations.

which lowers the energy barrier for wetting the volume between the pillars. The figure shows three steps in time to illustrate the movement of the liquid in the zipping regime. For moderate values of the height, this procedure leads to similar front velocities as those obtained after a spontaneous infiltration by placing the drop completely on the pillars. To highlight the overlap between the two methods, the front velocities from [23] were compared to the results obtained for the same geometries in this paper. Quantitative overlap was found. For a Kraton film with $h = 10 \mu$m and $a = 11 \mu$m, the initial method generated a front velocity of 0.7 ± 0.05 m/s [23], whereas the above-described method produces a front velocity of 0.8 ± 0.29 m/s (both methods averaged more than 9 recordings). This strategy allows us to collect data, even for those micro-patterns where the Wenzel state could not be observed with the initial method as the time until transition was longer than the evaporation time of the drop. The high-speed imaging was done with 10× magnification at 10000 fps. The measurements have been performed under standard lab conditions at $T = 20 \pm 2$ °C. Any variations in humidity did not influence the measurements significantly.

3 Results and discussion

A static drop that transits from the Cassie-Baxter state to the Wenzel state spontaneously is considered. The change in wetting state involves a contact line displacement and contact angle reduction. There is no rolling or sliding motion of the drop. During the wetting transition, the liquid-gas interface moving between the pillar pattern is followed and its velocity determined from high-speed movies. This front velocity v_f depends on the type of substrate (water contact angle θ), pillar height h, and gap size a between the pillars. All averaged experimental data points are displayed in fig. 3. At least 3 and up to 25 measurements

Table 2. Critical gap sizes a_c for different pillar heights h, obtained from eq. (2) and from experimental fitting.

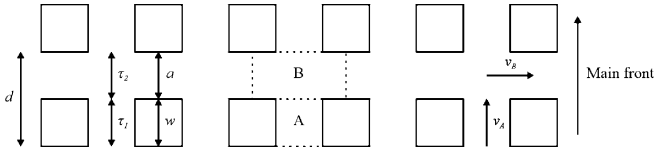| Material	h (μm)	a_c (eq. (2)) (μm)	a_c (exp) (μm)
Kraton	4.4	1.9	3.4
	10	4.2	5.1
	14	5.9	6.2
	15.6	6.6	6.2
PDMS	4.7	9.4	8.2
	8	16.0	18.9

Fig. 4. Illustration of the top view of twelve pillars with wavelength d (gap size a + pillar width w), timescales τ_1 and τ_2 and velocities v_A and v_B. The dotted lines mark the unit cell with subcells A and B.

were performed to generate each point (457 experiments in total). The data show that all three control parameters (a, h, and θ) influence the front velocity significantly. The velocity increases with increasing gap size a. For the same material and gap size the velocity decreases with increasing pillar height h. For a given geometry the velocity is reduced as the material displays a larger contact angle θ. As mentioned in the introduction, a critical point for front propagation can be defined by balancing the energy equations. The values for the critical gap size a_c for the different patterns described in this paper were calculated using eq. (2) (table 2). These values, below which no front propagation takes place, can also be obtained experimentally from the data (gap size at zero front velocity) in fig. 3. In the next sections, we describe the scaling of front velocities with geometrical (a and h) and material (θ) parameters.

3.1 Unitary cell approach

Based on the knowledge that there are two limiting cases with different characteristics (zipping and non-zipping), the presence of multiple scaling arguments is expected, each valid for its own regime. The unit cell is characterized by the sum of the volume between two pillars (area A, fig. 4, multiplied by pillar height h) and the volume beyond the pillars (area B times h). The difference in surface energies, derived purely from calculating interfacial areas before and after wetting this volume, can be written as

$$\Delta E_s = \sigma_{LG}(d^2 - w^2) + (\sigma_{SG} - \sigma_{LS})(d^2 - w^2 + 4wh)$$
$$= \sigma(d^2 - w^2)\left(1 + \cos\theta\left(\frac{d^2 - w^2 + 4wh}{d^2 - w^2}\right)\right), \quad (3)$$

with σ the surface tension of the liquid-air interface. This energy gain has to be balanced with the viscous dissipation

in the unit cell that we estimate with the volume integral of the velocity shear rate, estimated as v/l

$$\Delta E_d \simeq \int dV \eta \frac{v}{l} = h(d^2 - w^2)\eta\frac{v}{l}, \quad (4)$$

with $h(d^2 - w^2)$ the volume of the unit cell, η the dynamical viscosity of the liquid, v a characteristic velocity and l a characteristic length scale. The definition of l is crucial to understand the way the front velocity scales as a function of geometry and material properties [30]. As reported in our previous publications [23,26] and stated in appendix A, the 3D filling dynamics is very complex, including strong spatial anisotropies. If the gap size a is larger than the pillar height h, the shear rate is expected to be dominated by the vertical direction ($l \simeq h$). In the other limit ($a \ll h$) the shear rate is gap-dominated ($l \simeq a$). Due to the presence of the critical point, it is difficult to do experiments with gap sizes much smaller than the pillar height. The gap is usually larger than, or on the order of, the pillar height and therefore $l \simeq h$ is introduced in eq. (4). Balancing eqs. (3) and (4) with $l \simeq h$ leads to the front velocity as a function of geometry and wetting properties, which can be written as the dimensionless capillary number Ca

$$Ca = \frac{\eta v}{\sigma} \simeq 1 + \cos\theta\left(\frac{d^2 - w^2 + 4wh}{d^2 - w^2}\right). \quad (5)$$

This averaged capillary number is a measure of the averaged viscous forces per unit length (ηv) against the capillary forces per unit length (σ). This scaling argument is not generally valid though, and no data collapse is obtained using this expression. A simple estimate of the viscous integral as in eq. (4) does not take local variations in the velocity into account. The next section will address this point.

3.2 Two subcell approach

In the zipping regime ($a \simeq a_c$), the overall front velocity v_f can actually include two time scales τ_1, τ_2 with τ_1 being much smaller than τ_2 [26]. τ_1 equals the time needed to propagate between two pillars (fill volume A, fig. 4) and τ_2 equals the time needed to fill up the next row (volume B, fig. 4). Previously [23], only τ_1 was derived by matching surface energy with viscous dissipation between the pillars of subcell A

$$\tau_1 = \frac{t_0}{1 - \frac{\cos\theta}{\cos\theta_c}} = \frac{\eta h}{\sigma\left(1 + \cos\theta\left(\frac{2h+a}{a}\right)\right)}. \quad (6)$$

To obtain an overall front velocity, the residence time in both subcells has to be defined. For that a characteristic velocity is considered separately for each subcell (A and B). The in-plane velocity of the liquid in subcell A is defined as v_A and the liquid advances in the direction of the main front. The liquid in subcell B propagates in the direction perpendicular (in-plane) to the liquid in subcell A with a characteristic velocity v_B (fig. 4). Reformulating

the surface energy gain (derived again from purely interfacial area contributions, see figs. 4 and 1) and balancing that with the relative energy dissipation separately, one obtains for subcell A:

$$awh\eta\frac{v_A}{h} = \sigma aw\left(1 + \cos\theta\left(\frac{2h+a}{a}\right)\right) \qquad (7)$$

and for subcell B

$$adh\eta\frac{v_B}{h} = \sigma ad\left(1 + \cos\theta\left(\frac{2wh+da}{da}\right)\right). \qquad (8)$$

Hence there is a capillary number for each subcell

$$Ca_A = \frac{\eta v_A}{\sigma} = 1 + \cos\theta\left(\frac{2h+a}{a}\right), \qquad (9)$$

$$Ca_B = \frac{\eta v_B}{\sigma} = 1 + \cos\theta\left(\frac{2wh+da}{da}\right). \qquad (10)$$

It can be shown that $Ca_A \leq Ca_B$ is generally valid for a hydrophobic substrate ($\cos\theta < 0$), since

$$\frac{2h+a}{a} \geq \frac{2wh+da}{da} \qquad (11)$$

as $d \geq w$, because $d = a + w$. The conclusion is that filling up subcell B is never slower than filling up subcell A. In the zipping regime this difference in filling velocity between the two subcells is clearly observed. Volume B is filled much faster than volume A. Near the critical point the front between the pillars (in volume A) almost stops. In this limiting case $\cos\theta \to \cos\theta_c$ and the capillary numbers become

$$Ca_A = 1 - \left(\frac{a}{2h+a}\right)\left(\frac{2h+a}{a}\right) = 0, \qquad (12)$$

$$Ca_B = 1 - \left(\frac{a}{2h+a}\right)\left(\frac{2wh+da}{da}\right) > 0. \qquad (13)$$

By treating the two subcells separately, scaling arguments can be identified. The front velocity is evaluated in a unidirectional way: the filling is followed along a line between two rows of micro-pillars in the main front direction (fig. 4). The front velocity is thus defined in terms of distance that the front travels to fill up volume A and B, divided by the time it needs for that,

$$v_f = \frac{d}{\tau_1 + \tau_2} \simeq \frac{d}{\tau_A + \tau_B}, \qquad (14)$$

with τ_A the time scale corresponding to velocity v_A ($\tau_1 = \tau_A$) and τ_B to velocity v_B ($\tau_2 \simeq \tau_B$). From here on we distinguish between two limiting regimes. In the zipping regime ($a \simeq a_c$) time scale τ_A is much larger than time scale τ_B due to its divergence as stated before. The overall front velocity is therefore dominated by time scale τ_A (see appendix A). This time scale can be described as $\tau_A = w/v_A$ and can be combined with eq. (7) for subcell A.
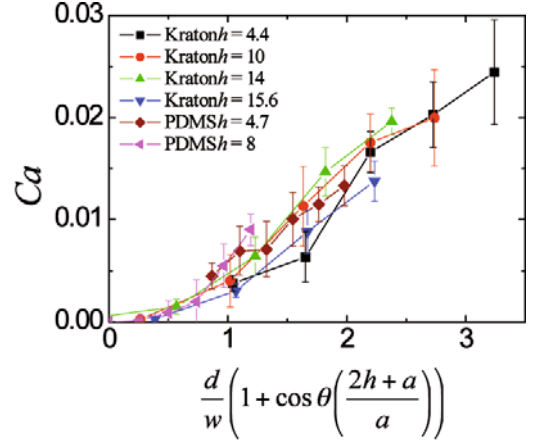

Fig. 5. Same data as fig. 3, but now plotted as capillary number Ca *versus* the scaling factor suggested by eq. (16) for the various materials and pillar heights h (given in μm). The data should give a universal curve in the zipping regime according to eq. (16).

The resulting equation for the front velocity in the zipping regime is

$$v_z \simeq \frac{d}{\tau_A + \tau_B} \simeq \frac{d}{\tau_A} = \frac{\sigma}{\eta}\frac{d}{w}\left(1 + \cos\theta\left(\frac{2h+a}{a}\right)\right), \qquad (15)$$

or rewritten in dimensionless terms as

$$Ca_z \simeq \frac{d}{w}\left(1 + \cos\theta\left(\frac{2h+a}{a}\right)\right). \qquad (16)$$

In the non-zipping regime a is much larger than a_c and the large-scale wetting pattern is more circular. This imposes that the velocities, v_A and v_B, are almost comparable, which gives

$$\frac{w}{\tau_a} \simeq \frac{a}{\tau_B}. \qquad (17)$$

Using the same approach as for the zipping regime, the overall non-zipping velocity becomes

$$v_{nz} \simeq \frac{d}{\tau_A + \tau_B} \simeq \frac{d}{\tau_A + \frac{a}{w}\tau_A} = \frac{\sigma}{\eta}\left(1 + \cos\theta\left(\frac{2h+a}{a}\right)\right) \qquad (18)$$

and in dimensionless form

$$Ca_{nz} \simeq 1 + \cos\theta\left(\frac{2h+a}{a}\right). \qquad (19)$$

Equations (16) and (19) express the core of our results, predicting a scaling behavior for the capillary number as a function of the geometry (a and h) and wetting properties (θ). For both scaling relations it holds that an increase in a (for fixed h and θ with $\theta > 90°$) produces an increase in capillary number Ca (increased velocity). An increase in h (for fixed a and θ with $\theta > 90°$) results in a decrease in Ca. These observations match the trends in the experimental data (fig. 3).

To assess the quantitative accuracy of eqs. (16) and (19), the scaling arguments are applied to the experimental data. In fig. 5 the rescaling for the zipping regime
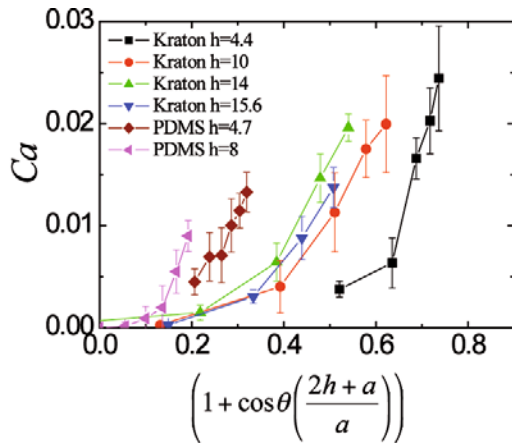
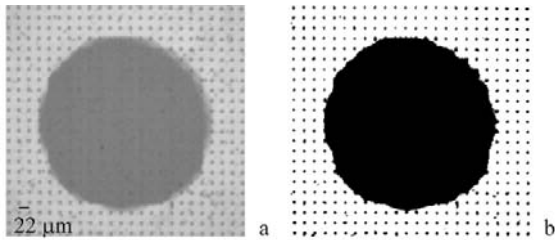**Fig. 6.** Same as fig. 5, but now plotted as suggested by eq. (19), which clearly does not display universal behavior.

Fig. 7. (a) Original image of one frame (exposure time $5\,\mu$s) during the wetting transition on a micro-patterned Kraton surface with $d = 22\,\mu$m and $h = 10\,\mu$m. The wetting front seems to be circular. (b) The same image with enhanced contrast. Now a step-like contour becomes visible at the liquid front.

(eq. (16)) is displayed. An excellent degree of collapse is observed for small gap sizes, where the zipping mechanism is expected to dominate. Even for larger gap sizes, where the filling is expected to be less influenced by the zipping mechanism, the proposed scaling argument still provides a good data collapse. Equation (16) reveals that the relevant geometrical parameters influencing the front velocity are the non-dimensional ratios d/w and h/a. Rescaling according to the non-zipping equation (eq. (19)) does not result in a collapse of the data (fig. 6). Indeed, at these gap sizes the wetted area still displays a step-like contour (fig. 7), which indicates that the zipping motion is still present. A pure non-zipping regime is expected for patterns with even larger gap sizes, involving front velocities beyond our experimental recording capabilities (probably in the order of $10\,$m/s).

4 Conclusions

A static drop transits spontaneously from the Cassie-Baxter state to the Wenzel state. The dynamics of this transition was measured and scaling arguments were developed. To explore the dynamics of this transition, several superhydrophobic micro-patterned polymeric surfaces were used. The geometry (pillar height and gap size) and material surface properties (water contact angle) of these
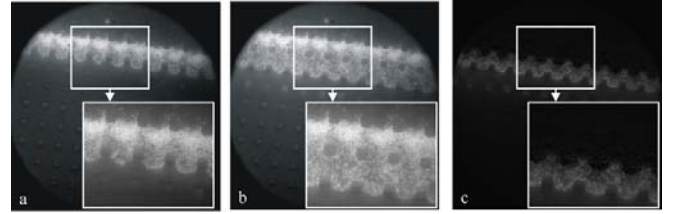

Fig. 8. (a, b) Two stills with blow-ups from a micro-particle imaging movie (two consecutive frames). (c) The difference between frames (a) and (b).

surfaces with square micro-pillars in a square array were varied extensively. The velocity of the wetting front increases with increasing gap size, decreasing pillar height or decreasing contact angle. The theoretically derived critical gap size, below which no transition occurs, is also observed in the experiments.

Balancing interfacial energy contributions with viscous dissipation yielded universal equations for the zipping and the transition dynamics. When using the height of the pillar as a characteristic length scale for the shear rate, good scaling is obtained with the argument for the zipping regime. Scaling arguments were also derived to determine whether the assumption of a horizontal characteristic length scale for the shear rate ($l \simeq w$) could be correct. This did not lead to any scaling for the set of experimental data, neither for the zipping nor for the non-zipping regime. The relevant parameters driving the front velocity are therefore the non-dimensional ratios d/w and h/a. These scaling arguments provide design criteria to tune the liquid velocity precisely on a micro-scale level. Future work will be devoted to exploring its practical use in the field of microfluidics, in particular by experimenting with other geometries and arrays of decreasing gap sizes.

Appendix A.

Seeding the liquid with fluorescent $0.3\,\mu$m polystyrene particles (R300 red fluorescing microspheres, Duke Scientific Corporation) as passive tracers shows that the liquid moves downwards in subcell B in the zipping regime (see fig. 8). It reveals the non-trivial filling dynamics in this regime involving two different time scales, in agreement with our previous experimental and numerical observations [23,26]. Figures 8a and b show two consecutive frames (n and $n+1$) of a movie with particles moving with the liquid that is wetting the micro-patterned film. The focal plane is located halfway along the height of the pillar and is approximately $1\,\mu$m thick. In the time between frame n and $n+1$ ($2\,$ms), the liquid front advances towards

the next row of pillars. In this same experiment it takes 36 ms before the front advances into the next row. Figure 8c displays the difference between the two frames by subtracting n from $n+1$. The first row is black, indicating that the particles located there did not move. Instead, additional particles are entering from the out-of-focus liquid reservoir above the micro-pattern. These findings indicate the filling of the volume from above, as opposed to filling from the side. Therefore, the accompanied shear rate is dominated by the vertical distance h.

References

1. D. Quéré, Rep. Prog. Phys. **68**, 2495 (2005).
2. X. Feng, L. Jiang, Adv. Mater. **18**, 3063 (2005).
3. X.M. Li, D. Reinhoudt, M. Crego-Calama, Chem. Soc. Rev. **36**, 1350 (2007).
4. X.M. Li, D. Reinhoudt, M. Crego-Calama, Chem. Soc. Rev. **36**, 1529 (2007).
5. W. Barthlott, C. Neinhuis, Planta **202**, 1 (1997).
6. C. Neinhuis, W. Barthlott, Ann. Bot. **79**, 667 (1997).
7. A.B.D. Cassie, S. Baxter, Trans. Faraday Soc. **40**, 546 (1944).
8. R.N. Wenzel, Ind. Engin. Chem. **28**, 988 (1936).
9. N.A. Patankar, Langmuir **19**, 1249 (2003).
10. A. Marmur, Langmuir **19**, 8343 (2003).
11. A. Marmur, Langmuir **20**, 3517 (2004).
12. J. Bico, C. Marzolin, D. Quéré, Europhys. Lett. **47**, 220 (1999).
13. N.A. Patankar, Langmuir **20**, 7097 (2004).
14. S. Moulinet, D. Bartolo, Eur. Phys. J. E **24**, 251 (2007).
15. H. Kusumaatmaja, J.M. Yeomans, Bull. Pol. Acad. Sci.: Tech. Sci. **55**, 203 (2007).
16. J. Bico, U. Thiele, D. Quéré, Colloids Surf. A: Physicochem. Engin. Asp. **206**, 41 (2002).
17. W. Li, A. Amirfazli, Adv. Colloid Interface Sci. **132**, 51 (2007).
18. L. Barbieri, E. Wagner, P. Hoffmann, Langmuir **23**, 1723 (2007).
19. G. McHale, N.J. Shirtcliffe, S. Aqil, C.C. Perry, M.I. Newton, Phys. Rev. Lett. **93**, 036102 (2004).
20. Y. Yu, Z.H. Zhao, Q.S. Zheng, Langmuir **223**, 8212 (2007).
21. B. He, N. A. Patankar, J. Lee, Langmuir **19**, 4999 (2003).
22. D. Oner, T.J. McCarthy, Langmuir **16**, 7777 (2000).
23. M. Sbragaglia, A.M. Peters, C. Pirat, B.M. Borkent, R.G.H. Lammertink, M. Wessling, D. Lohse, Phys. Rev. Lett. **99**, 156001 (2007).
24. J. Bico, C. Tordeux, D. Quéré, Europhys. Lett. **55**, 214 (2001).
25. A. Lafuma, D. Quéré, Nat. Mater. **2**, 457 (2003).
26. C. Pirat, M. Sbragaglia, A.M. Peters, B.M. Borkent, R.G.H. Lammertink, M. Wessling, D. Lohse, EPL **81**, 66002 (2008).
27. T. Cubaud, M. Fermigier, Europhys. Lett. **55**, 239 (2001).
28. T. Cubaud, M. Fermigier, J. Colloid Interface Sci. **269**, 171 (2004).
29. L. Courbin, E. Denieul, E. Dressaire, M. Roper, A. Ajdari, H.A. Stone, Nat. Mater. **6**, 661 (2007).
30. C. Ishino, M. Reyssat, E. Reyssat, K. Okumura, D. Quéré, EPL **79**, 56005 (2007).